JBC RESEARCH ARTICLE

The cytochrome *c* oxidase subunit COX6B1 is required for redox-sensitive early assembly and late stabilization of complex IV

Received for publication, July 28, 2025, and in revised form, November 26, 2025 Published, Papers in Press, December 17, 2025
https://doi.org/10.1016/j.jbc.2025.111070

Kristýna Čunátová[1,2,3], Marek Vrbacký[1], Michal Knězů[1], Alena Pecinová[1], Lukáš Alán[1,4], Josef Houštěk[1], Erika Fernández-Vizarra[2,3,5], Tomáš Mráček[1], and Petr Pecina[1,*]

From the [1]Laboratory of Bioenergetics, Institute of Physiology, Czech Academy of Sciences, Prague, Czech Republic; [2]Department of Biomedical Sciences, University of Padova, Padova, Italy; [3]Veneto Institute of Molecular Medicine, Padova, Italy; [4]Department of Biology, University of Padova, Padova, Italy; and [5]Department of Biochemistry and Molecular and Cellular Biology, University of Zaragoza, Huesca, Spain

Reviewed by members of the JBC Editorial Board. Edited by Ursula Jakob

COX6B1 is a nuclear-encoded subunit of the human mitochondrial cytochrome *c* oxidase (cIV) located in its intermembrane space–facing region. The relevance of COX6B1 in mitochondrial physiopathology was highlighted by the missense pathogenic variants associated with cIV deficiency. Despite the assigned COX6B1 role as a late incorporation subunit, the COX6B1 human cell line KO exhibited a total loss of cIV. To get a deeper insight into the mechanisms driving the lack of cIV assembly or destabilization in the absence of COX6B1, we used the COX6B1 KO cell background to express alternative oxidase and COX6B1 pathogenic variants. These analyses uncovered that the COX6B1 subunit is indispensable for redox-sensitive early cIV assembly steps, besides its contribution to the stabilization of cIV in the late assembly stages. In addition, we have evidenced the incorporation of partially assembled cIV modules directly into supercomplex structures, supporting the "cooperative assembly" model for respiratory chain biogenesis.

Human cytochrome *c* oxidase (complex IV [cIV], COX, EC 7.1.1.9) is the terminal component and pacemaker of the mitochondrial respiratory chain (RC) (1). cIV is found in the inner mitochondrial membrane in diverse forms—monomeric, dimeric (IV_2), and also participates in supramolecular structures interacting with other RC complexes I (cI) and dimeric III ($cIII_2$), forming the so-called supercomplexes (SCs, typically SC III_2IV, and respirasome—SC I III_2IV) (2). Human monomeric cIV is a protomer of three mitochondrial DNA (mtDNA)–encoded subunits (MT-CO1, MT-CO2, and MT-CO3) constituting its catalytic core and 11 supernumerary nuclear DNA (nDNA)–encoded subunits (COX4, COX5A, COX5B, COX6A, COX6B, COX6C, COX7A, COX7B, COX7C, COX8, and NDUFA4, alias COXFA4) (3–5), which are necessary for cIV assembly and maintenance. Seven of the nDNA-encoded subunits (COX4, COX6A, COX6B, COX7A, COX7B, COX8, and NDUFA4) exist in more than one variant, so-called isoforms, which are encoded by distinct genes (6, 7) and facilitate adaptation of cIV function in specific conditions and tissues (8, 9). Even if there are these tissue-specific differences in composition, cIV structure and subunit number are consistent (8, 10–13). In addition, the association of cIV within RC SCs might help fine-tune its function to specific conditions (8).

Originally, human cIV assembly was presumed as a sequential process, presenting with assembly intermediates defining the rate-limiting steps (14). This has been gradually refined resulting in the current "modular model" of *de novo* cIV assembly that implies individual modules (MT-CO1, MT-CO2, and MT-CO3)—each one formed by an mtDNA-encoded subunit accompanied by some of the nDNA-encoded subunits—that assemble in a process secured by a group of specific chaperons and assembly factors (AFs), all of them contributing toward the formation of a fully active cIV (Fig. 1*A*) (15–17). The incorporation of late-stage subunits, belonging to the MT-CO3 module, such as COX6A, COX6B, and COX7A, has been observed to happen not only during *de novo* cIV biogenesis but also as replacement of the components of previously assembled cIV structures (18). Moreover, several studies have presented that even incomplete cIV may attach to and stabilize SC I III_2 in the absence of a fully assembled cIV (12, 19–22). This indicates that parallel pathways of cIV assembly occur to form the monomeric cIV and the respirasome (20). These observations are consistent with the proposed "cooperative assembly" model, in which SC biogenesis is not the product of the association of fully assembled RC complexes but instead is the product of joining partially assembled modules of each component complex (23).

COX6B is an nDNA-encoded subunit associated with cIV facing the intermembrane space (IMS); it was thought to stabilize the dimeric cIV_2 structure and support the formation of the binding site for cytochrome *c* (4). While the ubiquitous mammalian isoform COX6B1 is present in all cell types and tissues, expression of the COX6B2 isoform is restricted to testes (24). The functional importance of this subunit is underscored by the existing link between decreased COX6B2

* For correspondence: Petr Pecina, petr.pecina@fgu.cas.cz.

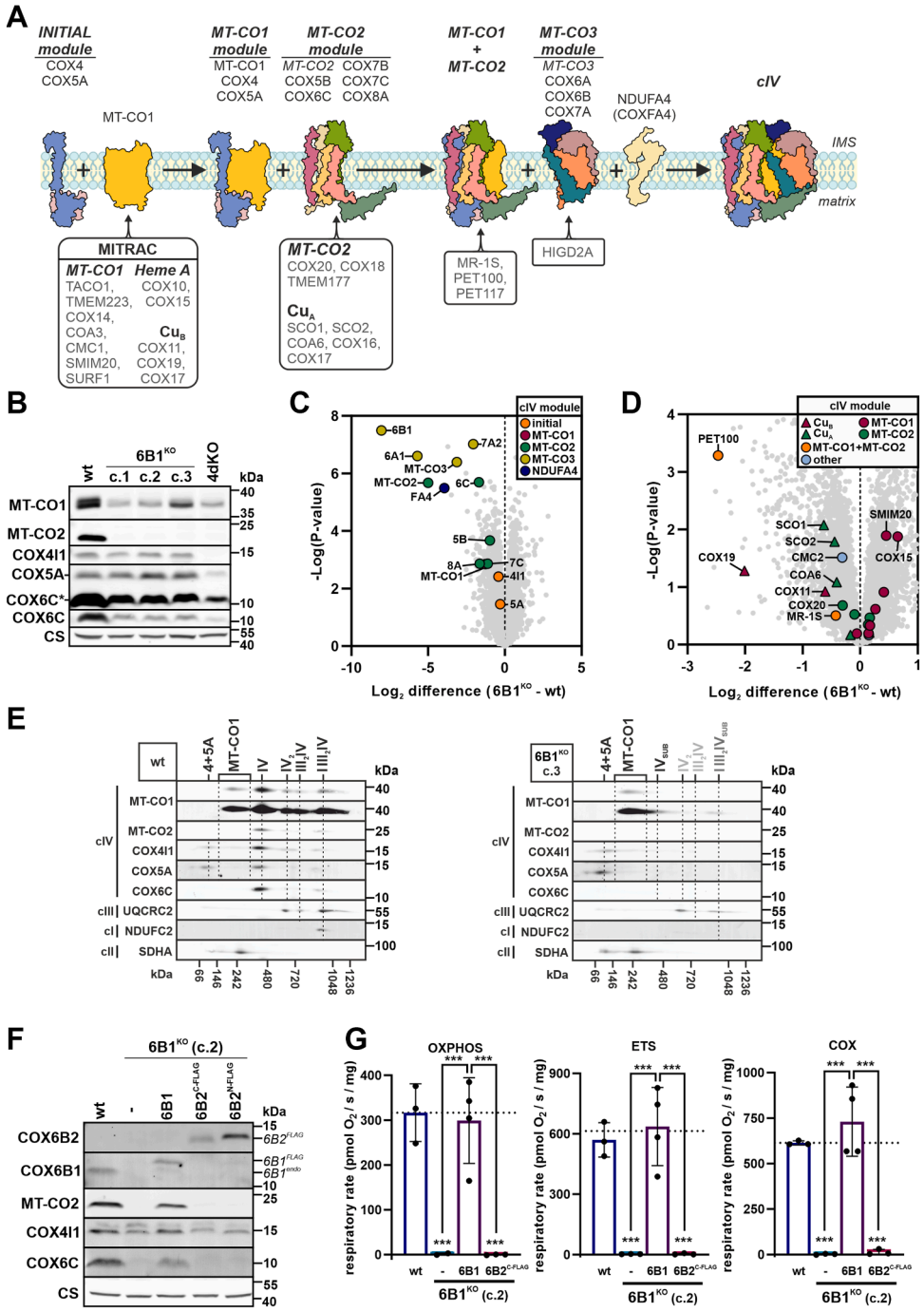

Figure 1. COX6B subunit is indispensable for early human cIV assembly and function. *A*, modular model of monomeric cIV assembly. Initially, the MT-CO1 module is formed by the connection of the initiating COX4–COX5A module with MT-CO1, which maturates in the MITRAC complex (mitochondrial translation regulation assembly intermediates of cytochrome *c* oxidase) (15, 80, 81). The second module consists of MT-CO2, which undergoes copper insertion, to form the binuclear Cu_A site, assisted by SCO1, SCO2, COX16, COX17, and COA6 chaperones, and subunits COX5B, COX6C, COX7B, and COX8A (39, 82–85). In the end, the third module containing MT-CO3, COX6A, COX6B, and COX7A subunits joins the nascent cIV under the assistance of HIGD2A, and the addition of NDUFA4 finalizes the assembly of a complete and fully functional cIV (12, 16, 34). cIV subunits are depicted in various colors and mentioned on the *top*; assembly factors (AFs) of individual modules are noted on the *bottom*. *Cartoons* are based on human cIV cryo-EM structure (PDB ID: 5Z62) (65). *B*, representative SDS-PAGE–WB analysis of the protein steady-state level of cIV subunits (MT-CO1, MT-CO2, COX4I1, COX5A, and COX6C) and citrate synthase (CS) as the loading control in whole-cell lysates of wt, $6B1^{KO}$ clones (c.1, c.2, and c.3), and COX4 KO (4dKO). COX6C* represents an overexposed signal of COX6C from the same image. See also quantification in Figure S1*A*. *C*, differential content of cIV subunits between wt and $6B1^{KO}$ cells. Volcano plot represents LFQ–MS analysis (wt: n = 4; $6B1^{KO}$ combines c.1, c.2, and c.3: n = 2 per each/n = 6 in total) of all analyzed proteins (*gray*), and subunits of cIV modules (initial: *orange*, MT-CO1: *magenta*, MT-CO2: *green*, MT-CO3: *yellow*, and NDUFA4: *blue*). COX6B1 protein missing in $6B1^{KO}$ was visualized; thanks to the imputation step (missing values replaced from normal distribution) performed during the Perseus analysis of the LFQ–MS data. For individual $6B1^{KO}$ clone data, see Figure S1*B*. *D*, differential content of cIV assembly factors (AFs) between wt and $6B1^{KO}$ cells. Volcano plot represents LFQ–MS analysis (wt: n = 4; $6B1^{KO}$ combines c.1, c.2, and c.3: n = 2 per each/n = 6 in total) of all analyzed proteins (*gray*), and cIV AFs (MT-CO1 metalation: *triangle in magenta*, MT-CO1 maturation: *circle in magenta*, MT-CO2 metalation: *triangle in green*, MT-CO2 maturation: *circle in green*, MT-CO1 + MT-CO2 metalation: *triangle in yellow*, MT-CO1 + MT-CO2 association: *circle in orange*, and other: *circle in blue*). For individual $6B1^{KO}$ clone data, see Figure S1*C*. *E*, 2D (BN/SDS)-PAGE–WB detection of cIV (MT-CO1, MT-CO2, COX4I1, COX5A, and COX6C antibodies), cIII (UQCRC2 antibody), and cI (NDUFC2 antibody) in wt

content and altered sperm motility and decreased fertility (25, 26). In addition, COX6B2 expression in other tissues might be associated with carcinogenesis (27–29).

Even though it is a peripherally associated subunit, COX6B1 is important for cIV structural stability/assembly or function—*COX6B1* missense pathogenic variants have been identified as the genetic cause of childhood-onset mitochondrial disease (30–32). The first two identified variants, R20C and R20H, led to a destabilization of COX6B1 interaction with cIV and decreased cIV activity. Similarly, the knockdown of *COX6B1* expression manifested as cIV deficiency (30). Therefore, based on multiple observations, the COX6B subunit was perceived as one of the subunits joining cIV assembly in the very late stages (12, 15, 33, 34). In contrast to this idea, we found that the KO of *COX6B1* in human cells produced a total loss of cIV (21), indicating an essential but largely unexplored role for COX6B1 in the early biogenesis of cIV.

Here, we have utilized *COX6B1* KO cells and subsequent models prepared by expression of its isoforms, its pathogenic variants (R20C and R20H), or alternative oxidase (AOX), which has allowed us to clarify the role of the COX6B1 subunit in the life cycle of cIV.

Results

COX6B subunit is indispensable for early human cIV assembly and function

We decided to generate COX6B1 KO as a model of late-stage cIV assembly disruption (15, 17) (Fig. 1*A*), which would contrast with the harsh COX4 KO models we generated previously (21, 35). For this purpose, we utilized CRISPR to knock out the *COX6B1* gene in human embryonic kidney 293 (HEK293) cells and identified a positive clone ($6B1^{KO}$, clone 2), which was characterized previously (21). In the present work, we included another two $6B1^{KO}$ clones (clone 1 and clone 3) to exclude clonal specificity and elucidate the reason for the severe cIV deficiency phenotype in COX6B1-lacking cells (21). Analysis of the steady-state level of cIV subunits in the three $6B1^{KO}$ clones (c.1, c.2, and c.3) by SDS-PAGE/Western blot (WB) (Figs. 1*B*, S1*A*) consistently revealed the downregulation of numerous cIV subunits. MT-CO1 and COX6C subunits were significantly decreased compared with wt cells, and MT-CO2 was completely undetectable in $6B1^{KO}$, as in the severe cIV deficiency model 4dKO (KO of the early assembly COX4 subunit) (35). On the contrary, the levels of COX4 and COX5A subunits in $6B1^{KO}$ were similar to wt, suggesting preservation of the early assembly intermediate of cIV (Figs. 1*B*, S1*A*). This finding was confirmed and extended by whole proteome analysis of three $6B1^{KO}$ clones and the wt cells, using label-free quantification–mass spectrometry (LFQ–MS). The levels of MT-CO3 module subunits (MT-CO3, COX6A1, and COX7A2) and NDUFA4 were the most decreased, but MT-CO2 module subunits, MT-CO2 and COX6C, were also significantly reduced in COX6B1-lacking cells (Figs. 1*C*, S1*B*). The LFQ–MS data for cIV AFs in the three $6B1^{KO}$ clones revealed a significant decrease of PET100, which is thought to secure the stability of MT-CO2 joining the MT-CO1 module (15) (Figs. 1*D*, S1*C*). Apart from PET100, the most decreased AFs were those involved in MT-CO1 (COX19 and COX11) and MT-CO2 (SCO1, SCO2, and COA6) metalation (Fig. 1*D*). Altogether, these results suggest a block in cIV assembly at the stage of MT-CO2 maturation and/or incorporation.

To inspect the *COX6B1* KO effect on the native cIV forms and their assembly intermediates, we performed a first-dimension Blue Native electrophoresis (BN-PAGE) followed by a denaturing (SDS-PAGE) second dimension and WB immunodetection analysis. These experiments showed the total loss of fully assembled monomeric cIV (IV), cIV dimer (IV_2), as well as SC III_2IV in $6B1^{KO}$. Nevertheless, several cIV assembly intermediates were accumulated in $6B1^{KO}$ clones in comparison to wt (Fig. 1*E*—clone 3, *cf.* also 4C—clone 2, S3B—clone 1). The most prominent assembly intermediates in $6B1^{KO}$ cells, composed of subunits MT-CO1, COX4, and COX5A, correspond to the MT-CO1 module, the initial intermediate (COX4 + COX5A), and their association, preceding the incorporation of the MT-CO2 module. In addition, a signal corresponding to MT-CO1 could be detected in the higher molecular weight part of the blot (at ∼1 MDa) in the $6B1^{KO}$ samples and comigrating with $cIII_2$ (Fig. 1*E*). This implies a non-negligible presence of SC species formed by cI, the dimer of cIII, and at least MT-CO1.

To test whether the *COX6B1* KO phenotype could be rescued not only by overexpression of COX6B1 but also by the COX6B2 isoform, we stably expressed either COX6B1 or COX6B2 in the $6B1^{KO}$ clone 2 (Fig. 1*F*). The complementation of $6B1^{KO}$ by a C-terminal FLAG-tagged COX6B1 ($6B1^{KO}$ + 6B1) resulted in a significant recovery of the MT-CO2 and COX6C levels (Figs. 1*F*, S1*D*). This was paralleled by the restoration of respiratory capacities of COX as well as of the oxidative phosphorylation (OXPHOS) and electron transporting system (ETS) states to levels comparable to the wt (Fig. 1*G*; details of the respirometry protocol are described in Fig. S1*E*). On the other hand, the expression of either a C-terminal or an N-terminal FLAG-tagged COX6B2 isoform failed to even marginally rescue either MT-CO2 levels (Figs. 1*F*, S1*D*) or mitochondrial respiration (Fig. 1*G*). This may indicate that other cIV tissue-specific isoforms and/or

(*left*) and $6B1^{KO}$ (c.3, *right*) mitochondrial fraction. Antibody against cII (SDHA) was used as a loading control. *F*, representative SDS-PAGE–WB analysis of the protein steady-state level of cIV subunits (COX6B2, COX6B1, MT-CO2, COX4I1, and COX6C) and citrate synthase (CS) as the loading control in whole-cell lysates of wt, $6B1^{KO}$, $6B1^{KO}$ + 6B1, $6B1^{KO}$ + $6B2^{C\text{-}FLAG}$, and $6B1^{KO}$ + $6B2^{N\text{-}FLAG}$. FLAG-tagged COX6B1 and COX6B2 proteins are marked by $6B1^{FLAG}$ and $6B2^{FLAG}$, respectively; endogenous COX6B1 is labeled with $6B1^{endo}$ (in *italics*). See also quantification in Figure S1*D*. *G*, respiratory rates representing maximal capacities of OXPHOS, ETS, and COX measured in digitonin-permeabilized cells (0.4–1.5 mg of protein) are plotted as the mean ± SD value for wt (n = 3), $6B1^{KO}$ (n = 2), $6B1^{KO}$ + 6B1 (n = 4), and $6B1^{KO}$ + $6B2^{C\text{-}FLAG}$ (n = 3). One-way ANOVA (***$p < 0.001$) was performed. Representative traces with indicated additions of substrates and inhibitors are shown in Figure S1E. cI/III/IV, complex I/III/IV; COX, cytochrome *c* oxidase; ETS, electron transporting system; LFQ–MS, label-free quantification–mass spectrometry; OXPHOS, oxidative phosphorylation; PDB, Protein Data Bank.

other factors are required for COX6B2 incorporation into cIV. At the same time, it explains why COX6B2 upregulation cannot functionally complement pathologic COX6B1 variants in patients, since the same is likely valid also for tissues other than testes.

The presented data indicate that the COX6B1 subunit is essential for proper cIV assembly and function, since its loss leads to total cIV deficiency caused by a block in cIV biogenesis at a stage subsequent to MT-CO1 + COX4 + COX5A subassembly formation.

R20C pathogenic variant of COX6B1 affects an early cIV assembly, unlike R20H that disrupts cIV stability

Interestingly, the cIV assembly defect observed in patients carrying homozygous pathogenic variants in COX6B1 is much milder than the defect in the 6B1^{KO} cells (30). Therefore, we next explored the effects of the R20H and R20C COX6B1 pathogenic variants (Fig. 2, *A* and *B*) when expressed in the HEK293 6B1^{KO} cell line. The expression levels of a C-terminal FLAG-tagged COX6B1 R20H variant (6B1^{KO} + R20H) were comparable to those of the wt COX6B1 (6B1^{KO} + 6B1, Figs. 2*C*, S2). In contrast, the overexpression of a C-terminal FLAG-tagged R20C variant (clone 2, to produce 6B1^{KO} + R20C) resulted in much lower COX6B1 levels, most probably because of a decreased stability of the R20C variant (Figs. 2*C*, S2). The levels of the MT-CO2 subunit were decreased in both 6B1^{KO} + R20H and 6B1^{KO} + R20C cells compared with 6B1^{KO} + 6B1, whereas COX6C content was the same in the three cell lines, being decreased relative to wt (Figs. 2*C*, S2). COX4 subunit levels were the same in the five cell lines (wt, 6B1^{KO}, and the three overexpression lines) (Figs. 2*C*, S2).

The cIV defect observed in cells expressing the two different R20 variants was not equivalent, as the R20C induced a harsher assembly defect with only a little detectable amount of the cIV monomer and undetectable cIV dimer (IV_2) and SC III_2IV (Fig. 2*D*). Interestingly enough, MT-CO1 was detected in the respirasome in both R20C and R20H cell lines (Fig. 2*D*). The milder cIV assembly defect was also reflected with higher levels of respiration (coupled—OXPHOS, uncoupled—ETS state, and cIV capacity—COX) in the 6B1^{KO} + R20H than in the 6B1^{KO} + R20C, which, despite the very low abundance of fully assembled cIV native forms, could sustain detectable levels of oxygen consumption. Specifically, the respiration rates were approximately 2.5 and 3 times decreased in the ETS (maximal respiratory capacity after uncoupling) state in 6B1^{KO} + R20H and 6B1^{KO} + R20C, respectively, compared with wt and 6B1^{KO} + 6B1 cell lines (Fig. 2*E*). Thus, the introduction of the R20C variant disrupted cIV native forms and respiration to a greater extent than R20H, similar to the observations in patient-derived fibroblasts (30, 31). Interestingly, the additional cysteine residue in the COX6B1-R20C variant forms an artificial Cx9C motif adjacent to the one in the COX6B1 wt primary sequence (Fig. 2*F*). This is likely to interfere with proper folding within the IMS (36), resulting in decreased stability and lower steady-state levels of the protein (Figs. 2*C*, S2).

To reveal the ability of R20C and R20H variants to associate with the native cIV forms, as well as their effect on cIV subunit and AF amounts, we used the mild detergent digitonin to solubilize the mitochondrial membranes and performed immunoprecipitation of cIV, followed by MS analysis of the co-immunopurified fractions (Fig. 3). According to these analyses, the same cIV structural subunits were found reduced in 6B1^{KO} + R20H, 6B1^{KO} + R20C, and 6B1^{KO} compared with wt but not to the same degree (Fig. 3*A*). The initial module was least affected (COX4 and COX5A being unchanged), and MT-CO1 was within the least decreased subunits. MT-CO2 module subunits were, on average, under-represented to a larger extent, and MT-CO3 plus NDUFA4 were the most affected (Fig. 3*A*). In concordance with the previous results (Fig. 2, *C* and *D*), 6B1^{KO} + R20C showed a more profound decrease of subunits incorporated into the native cIV subassemblies, including COX6B1 (containing the variant), in comparison with 6B1^{KO} + R20H (Fig. 3*A*). Analysis of cIV-bound AFs showed higher association of CMC1, COX14, and COA3, which stabilize MT-CO1 ahead of MT-CO2 incorporation and metalation, and lower abundance of PET100 in 6B1^{KO}, but also in 6B1^{KO} + R20H and 6B1^{KO} + R20C compared with wt (Fig. 3*B*). Strikingly, the level of bound COA6, a factor responsible for copper delivery to MT-CO2 (37–39), was increased in the case of 6B1^{KO} + R20H and 6B1^{KO} + R20C models, whereas being decreased in 6B1^{KO} in comparison to wt (Fig. 3*B*). This difference reinforces the possibility of the COX6B1 subunit having relevance for MT-CO2 maturation. Further, the difference between R20C and R20H variants of COX6B1 was highlighted by diverse alterations of cIV-bound AFs, ensuring MT-CO1 and MT-CO2 metalation and maturation, which were diminished in 6B1^{KO} + R20C relative to 6B1^{KO} + R20H (Fig. 3*B*).

Expression of AOX restores cIV assembly with negligible cIV function in COX6B1-deficient cells

Our data indicate a block at the level of MT-CO2 maturation in 6B1^{KO} cells. Since MT-CO2 maturation is a redox-sensitive process (40, 41) we modified the redox status in the 6B1^{KO} mitochondria *via* xenoexpression of an AOX, an enzyme with CoQ:O_2 oxidoreductase activity present in the mitochondria of certain organisms (21, 42, 43). SDS-PAGE–WB analysis showed that stable expression of AOX in 6B1^{KO} (6B1^{KO} + AOX, c.1, and c.2) led to a significant increase in the steady-state level of the cIV subunits most profoundly decreased in 6B1^{KO} (MT-CO1, MT-CO2, and COX6C) (Figs. 4*A*, S3*A*). In more detail, LFQ–MS analysis of 6B1^{KO} + AOX compared with 6B1^{KO} showed a remarkable increase of the MT-CO2 module subunits (MT-CO2, COX5B, and COX7C), whereas the rest of the cIV subunits showed a milder increase after AOX expression (Fig. 4*B*). Interestingly, the proteomic analysis revealed a major increase in PET100, which was the most downregulated cIV AF in 6B1^{KO} compared with wt (Fig. 1*D*). In addition, the AFs, COX19,

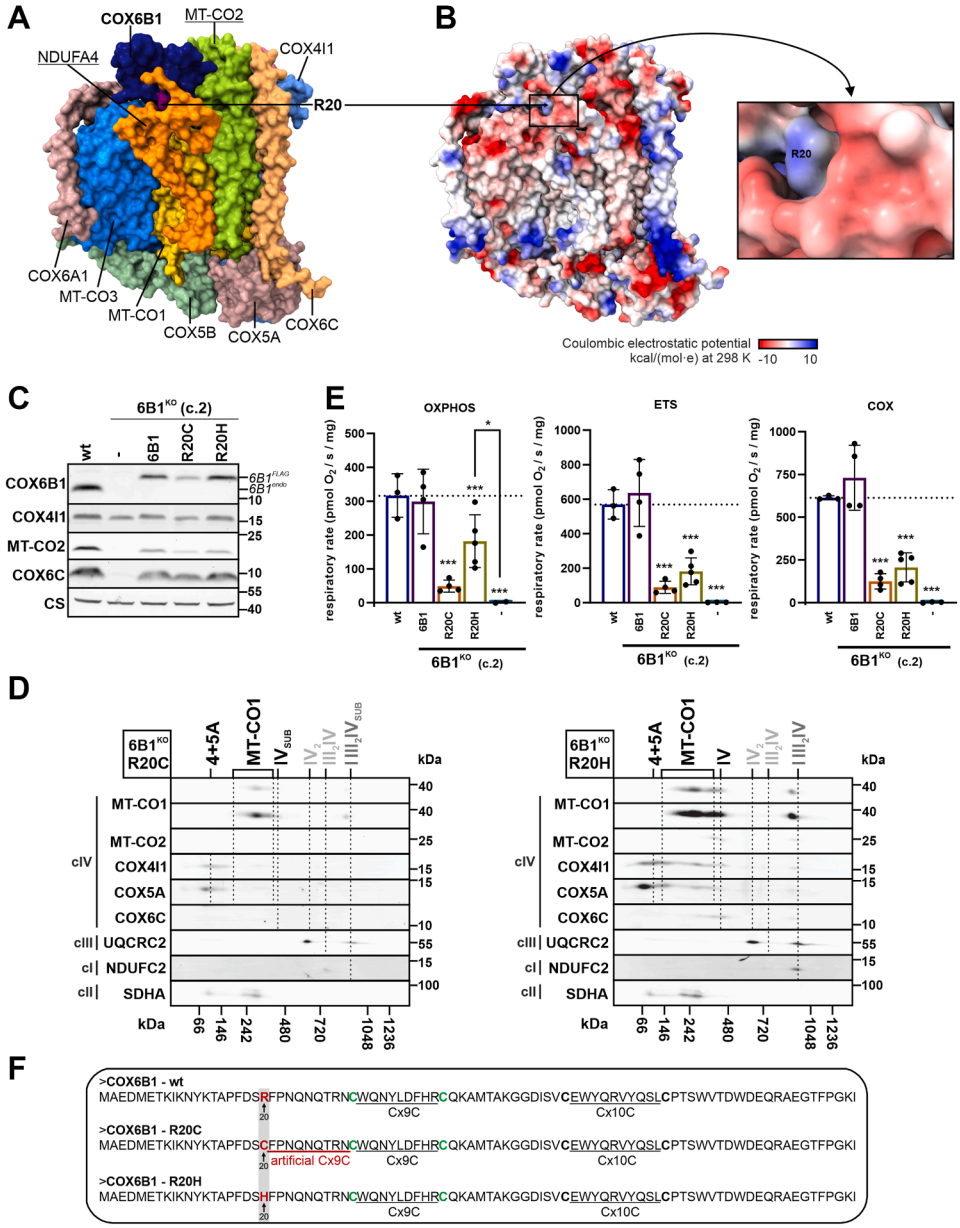

Figure 2. Characterization of R20C and R20H pathogenic variants of COX6B1 in HEK293 cellular models. *A*, position of COX6B1 R20 in human cIV structure. Structural subunits of cIV are indicated in different colors, with emphasis on the location of R20 (*violet*) of COX6B1 (*dark blue*) in the cryo-EM structure of human cIV (PDB ID: 5Z62) (65). The image was created using UCSF ChimeraX (86, 87). *B*, structure of cIV monomer (*left*) and detailed image of COX6B1—R20 (*right*) using coulombic electrostatic potential visualization (by generic ChimeraX-embedded command: coulombic), based on human cIV structure (PDB ID: 5Z62). The images were created with UCSF ChimeraX (86, 87). *C*, representative SDS-PAGE–WB analysis of the protein steady-state level of cIV subunits (COX6B1, COX4I1, MT-CO2, and COX6C) and citrate synthase (CS) as the loading control, in whole-cell lysates of wt, 6B1^{KO}, 6B1^{KO} + 6B1, 6B1^{KO} + R20C, and 6B1^{KO} + R20H. FLAG-tagged COX6B1 and endogenous COX6B1 proteins are marked with 6B1^{FLAG} and 6B1^{endo} (in *italics*), respectively. See also quantification in Figure S2. *D*, 2D (BN/SDS)-PAGE–WB detection of cIV (MT-CO1, MT-CO2, COX4I1, COX5A, and COX6C antibodies), cIII (UQCRC2 antibody), and cI (NDUFC2 antibody) in 6B1^{KO} + R20C (*left*) and 6B1^{KO} + R20H (*right*) mitochondrial fraction. Antibody against cII (SDHA) was used as a loading control. *E*, respiratory rates representing maximal capacities of OXPHOS, ETS, and COX measured in digitonin-permeabilized cells (0.4–1.5 mg of protein) are plotted as the mean ± SD value for wt (n = 3), 6B1^{KO} + 6B1 (n = 4), 6B1^{KO} + R20C (n = 4), 6B1^{KO} + R20H (n = 5), and 6B1^{KO} (n = 2). One-way ANOVA (*$p < 0.05$, ***$p < 0.001$) was performed. Plotted data of wt, 6B1^{KO}, and 6B1^{KO} + 6B1 originate from Figure S1*G*. *F*, primary sequence of wt, R20C, and R20H variants of COX6B1 protein showing its natural Cx9C and Cx10C motifs and the respective position of R20. The artificial Cx9C motif created by the R20C pathogenic variant is highlighted in *red*. BN-PAGE, Blue Native PAGE; cI/III/IV, complexes I/III/IV; COX, cytochrome *c* oxidase; ETS, electron transporting system; HEK293, human embryonic kidney 293 cell line; OXPHOS, oxidative phosphorylation; PDB, Protein Data Bank.

COX11, and MR-1S, were also increased in 6B1^{KO} + AOX (Fig. 4*B*). In accordance, 2D BN–SDS-PAGE followed by WB showed increased incorporation of cIV subunits (MT-CO1, COX4, COX5A, MT-CO2, and COX6C) into the assembly intermediate IV$_{sub}$ in 6B1^{KO} + AOX compared with 6B1^{KO}, indicating that AOX-mediated alleviation of the reductive stress associated with cIV deficiency allows cIV assembly to proceed, specifically permitting the incorporation of MT-CO2 (Figs. 4, *C* and *D*, S3*B*). The abundance of both MT-CO1 and all the other tested cIV subunits in SC I III$_2$IV$_{sub}$ was also

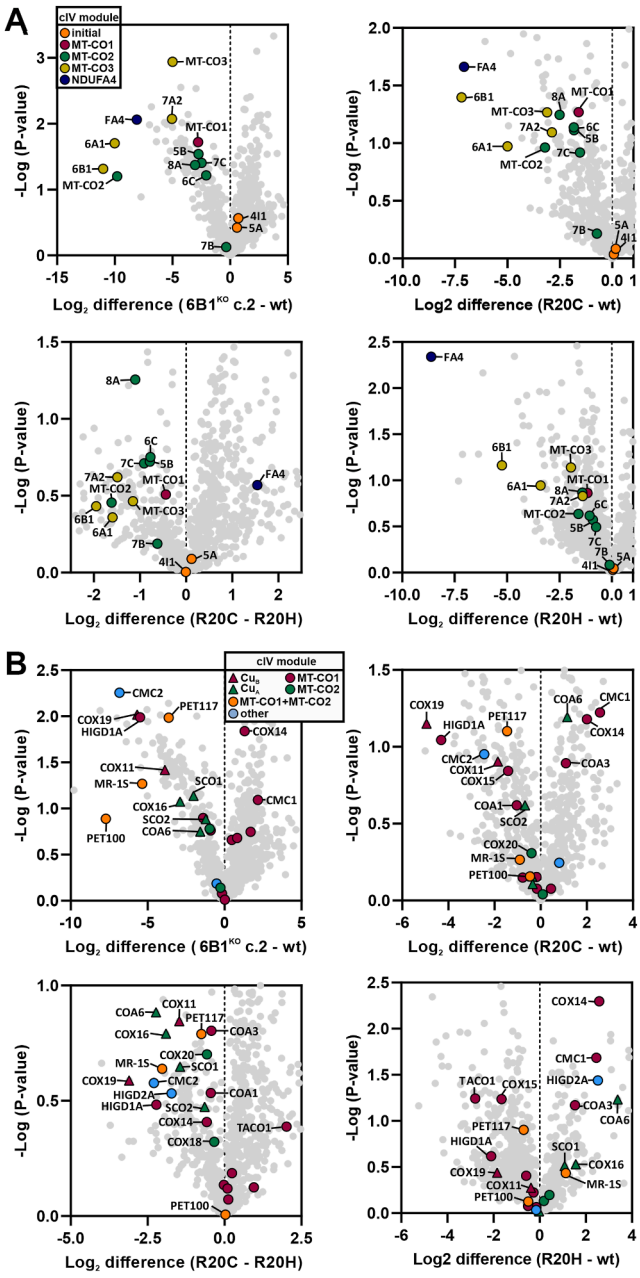

Figure 3. R20C pathogenic variant of COX6B1 affects an early cIV assembly, unlike R20H that disrupts cIV stability. *A*, differential amount of cIV subunits associated in cIV forms between wt and 6B1^{KO} (*top left*), 6B1^{KO} + R20C (*top right*), 6B1^{KO} + R20H (*bottom right*), and between 6B1^{KO} + R20C and 6B1^{KO} + R20H (*bottom left*). Volcano plots represent LFQ–MS analysis (n = 2) of all detected proteins (*gray*) and subunits of cIV modules (initial: *orange*, MT-CO1: *magenta*, MT-CO2: *green*, MT-CO3: *yellow*, and NDUFA4: *blue*). COX6B1 protein missing in 6B1^{KO} was visualized; thanks to the imputation step (missing values replaced from a normal distribution) performed during the Perseus analysis of the LFQ–MS data. *B*, differential amount of cIV AFs associated with cIV forms between wt and 6B1^{KO} (*top left*), 6B1^{KO} + R20C (*top right*), 6B1^{KO} + R20H (*bottom right*), and between 6B1^{KO} + R20C and 6B1^{KO} + R20H (*bottom left*). Volcano plots represent LFQ–MS analysis (n = 2) of all detected proteins (*gray*) and cIV assembly factors (MT-CO1 metalation: *triangle in magenta*, MT-CO1 maturation: *circle in magenta*, MT-CO2 metalation: *triangle in green*, MT-CO2 maturation: *circle in green*, MT-CO1 + MT-CO2 metalation: *triangle in yellow*, MT-CO1 + MT-CO2 association: *circle in orange*, and other: *circle in blue*). cIV, complex IV; COX, cytochrome *c* oxidase; LFQ–MS, label-free quantification–mass spectrometry.

substantially augmented after AOX expression compared with 6B1^{KO}, whereas IV_2 and III_2IV SCs remained absent (Figs. 4, *C* and *D*, S3*B*). Next, we examined whether the cIV forms assembled in 6B1^{KO} + AOX were respiratory competent. Even though the AOX-expressing cells displayed robust rates of routine respiration, titration of the AOX inhibitor (salicylhydroxamic acid) completely abolished oxygen consumption, indicating that in intact cells, oxygen consumption was exclusively happening through AOX (Fig. S3, *C* and *D*). Subsequent supplementation of respiratory substrates into digitonin-permeabilized 6B1^{KO} + AOX could not sustain significant oxygen consumption, again indicating an almost complete lack of respiration through cIV in these cells (Fig. 4*E*). However, a low, yet still detectable, respiration through cIV (COX) after supplementation with the artificial substrates ascorbate + tetramethylphenylenediamine (TMPD) (corrected for the potassium cyanide [KCN]–insensitive portion) was observed in 6B1^{KO} + AOX (Fig. S3*C*), contrasting with 6B1^{KO} (Fig. 4*F*). This means that IV_{sub} present in 6B1^{KO} is catalytically competent, yet with only very limited activity, accounting only for approximately 5% of the rate in wt cells.

To characterize the precise composition of the accumulated cIV assembly intermediates and the partial respirasome (SC I III_2IV_{sub}) in parental 6B1^{KO} cells and those expressing AOX, we performed proteomics-based complexome profiling analysis (44) (Figs. 5, *A* and *B*, S4*A*). wt cells showed uniform distribution of the 13 detected cIV subunits into all the mature cIV-containing species, whereas in 6B1^{KO}, eight early assembling subunits mostly accumulated in assembly intermediates (Fig. 5*A*). Interestingly, a number of cIV subunits (COX4I1, MT-CO2, and COX7A2) were detected within the SC I III_2IV_{sub} in the 6B1^{KO} by complexome profiling. This indicates the incorporation of partially assembled cIV modules directly on the SC platform running in parallel with the assembly of the individual complex, which is consistent with the "cooperative assembly" model of RC biogenesis (23). In 6B1^{KO} cells expressing AOX, additional cIV subunits (including MT-CO3) were present in higher quantities in the SC I III_2IV_{sub}, only lacking a few late assembling cIV subunits (COX7C, COX8A, COX6A, and NDUFA4), apart from the genetically removed COX6B1 (Fig. 5, *A* and *B*). In addition to the early assembly intermediates, the cIV subassembly (IV_{sub}) containing almost all cIV subunits was also present in 6B1^{KO} + AOX. Notably, the subunits detected in IV_{sub} belong to all three assembly modules, and the only ones lacking were COX8A, COX6A, and NDUFA4 (Fig. 5*A*). These observations indicate that both the IV_{sub} and the SC I III_2IV_{sub} represent the genuine and the most complex cIV species that can be assembled in the absence of COX6B1 in redox conditions that circumvent the assembly block associated with the absence of this particular subunit.

The complexome profiling results correlated with MS analysis of immunocaptured cIV, which showed a higher level of MT-CO2 and MT-CO3 module subunits bound to the

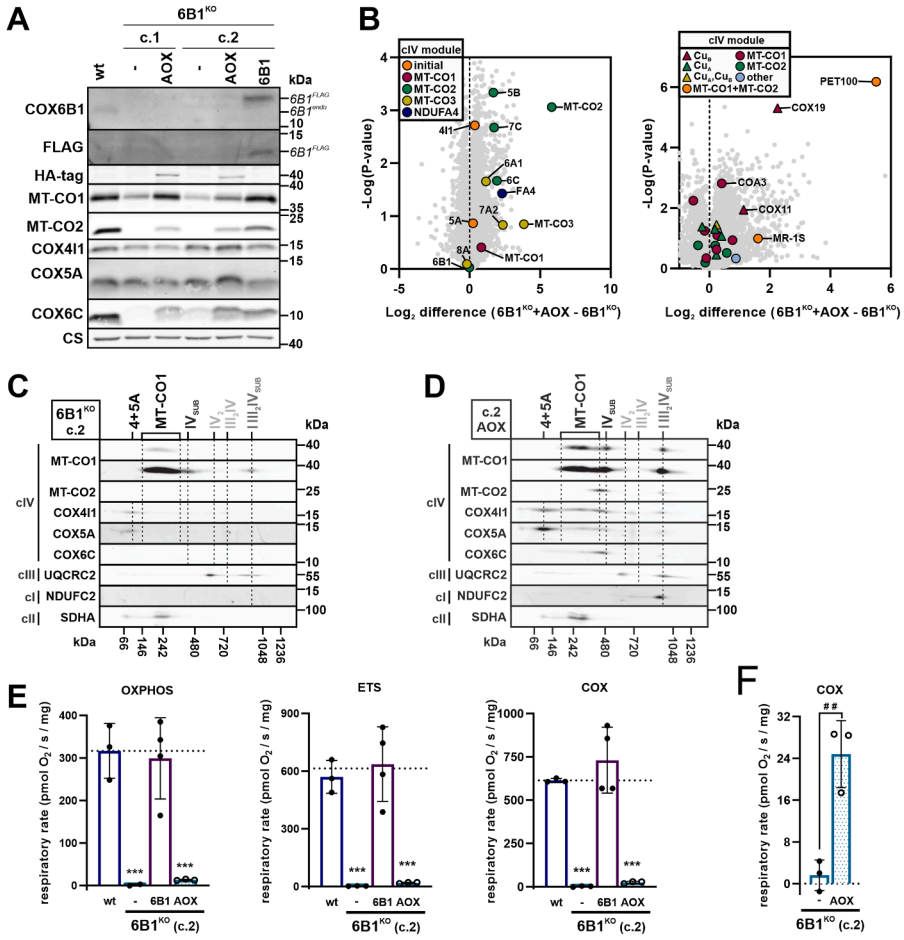

Figure 4. Expression of alternative oxidase (AOX) restores cIV assembly intermediate formation with negligible cIV function in COX6B1-deficient cells. *A*, representative SDS-PAGE–WB analysis of the protein steady-state level of cIV subunits (MT-CO1, MT-CO2, COX4I1, COX5A, COX6B1, and COX6C), C-terminal FLAG-tagged COX6B1 (FLAG antibody), HA-tagged AOX (HA-tag antibody), and citrate synthase (CS) as the loading control in whole-cell lysates of wt, 6B1^{KO} c.1, 6B1^{KO} c.1 + AOX, 6B1^{KO} c.2, 6B1^{KO} c.2 + AOX, and 6B1^{KO} + 6B1. FLAG-tagged COX6B1 and endogenous COX6B1 proteins are marked with 6B1^{FLAG} and 6B1^{endo} (in *italics*), respectively. See also quantification in Figure S3*A*. *B*, differential content of cIV subunits and assembly factors (AFs) between 6B1^{KO} and 6B1^{KO} + AOX cells. Volcano plots represent LFQ–MS analysis (6B1^{KO} c.2: n = 3, 6B1^{KO} + AOX: n = 3) of all analyzed proteins (*gray*) and subunits of cIV modules (initial: *orange*, MT-CO1: *magenta*, MT-CO2: *green*, MT-CO3: *yellow*, and NDUFA4: *blue*) on the *left*, cIV assembly factors (MT-CO1 metalation: *triangle in magenta*, MT-CO1 maturation: *circle in magenta*, MT-CO2 metalation: *triangle in green*, MT-CO2 maturation: *circle in green*, MT-CO1 + MT-CO2 metalation: *triangle in yellow*, MT-CO1 + MT-CO2 association: *circle in orange*, and other: *circle in blue*) on the *right*. COX6B1 protein missing in 6B1^{KO} was visualized; thanks to the imputation step (missing values replaced from normal distribution) performed during the Perseus analysis of the LFQ–MS data. *C*, 2D (BN/SDS)-PAGE–WB detection of cIV (MT-CO1, MT-CO2, COX4I1, COX5A, and COX6C antibodies), cIII (UQCRC2 antibody), and cI (NDUFC2 antibody) in 6B1^{KO} c.2 mitochondrial fraction. Antibody against cII (SDHA) was used as a loading control. For 6B1^{KO} c.1, see also Figure S3*B*. *D*, 2D (BN/SDS)-PAGE/WB detection of cIV (MT-CO1, MT-CO2, COX4I1, COX5A, and COX6C antibodies), cIII (UQCRC2 antibody), and cI (NDUFC2 antibody) in 6B1^{KO} + AOX mitochondrial fraction. Antibody against cII (SDHA) was used as a loading control. For 6B1^{KO} c.1 + AOX, see also Figure S3*B*. *E*, respiratory rates representing maximal capacities of OXPHOS, ETS, and COX measured in digitonin-permeabilized cells (0.4–1.5 mg of protein) are plotted as the mean ± SD value for wt (n = 3), 6B1^{KO} (n = 3), 6B1^{KO} + 6B1 (n = 4) and (n = 3). One-way ANOVA (***$p < 0.001$) was performed. Plotted data of wt, 6B1^{KO}, and 6B1^{KO} + 6B1 originate from Figure S1*G*. Representative traces of oxygen consumption in 6B1^{KO} + AOX in the presence of the AOX inhibitor SHAM or the cIV inhibitor KCN are shown in Figure S3, *C* and *D*, respectively. *F*, respiratory capacity in COX state plotted as the mean ± SD value of 6B1^{KO} (n = 3) and 6B1^{KO} + AOX (n = 3). Unpaired, two-tailed *t* test (##$p < 0.01$) was performed. The graph represents *y*-axis zoomed-in representation of 6B1^{KO} and 6B1^{KO} + AOX rates displayed in Figure S4*E*. cI/III/IV, complexes I/III/IV; COX, cytochrome *c* oxidase; ETS, electron transporting system; KCN, potassium cyanide; LFQ–MS, label-free quantification–mass spectrometry; OXPHOS, oxidative phosphorylation; SHAM, salicylhydroxamic acid.

native cIV forms in 6B1^{KO} + AOX relative to 6B1^{KO}, with the exception of COX6A1 and NDUFA4 subunits (Fig. 5*C*). Moreover, another sign of restored MT-CO2 maturation and assembly after AOX expression in 6B1^{KO} was represented by augmented association of redox-sensitive AFs governing copper delivery to MT-CO2, that is, SCO1, SCO2, COA6, and COX16, as well of the chaperones involved in MT-CO2 module incorporation (PET100, PET117, and MR-1S) (Fig. 5*D*). Interestingly, COA6, PET100, and other AFs were more abundant in 6B1^{KO} + AOX than in wt, indicating persisting nonoptimal assembly conditions in the absence of COX6B1, despite redox balance normalization by AOX (Fig. 5*D*). This was specifically observed in the case of PET100 by complexome profiling, which was absent in 6B1^{KO}, accumulated in the cIV monomer in wt, but was readily accumulated within IV_{sub} and I III_2IV_{sub} in 6B1^{KO} + AOX (Fig. 5*A*). In addition, very low amounts of COX6A and NDUFA4 were immunocaptured with cIV in 6B1^{KO} compared with the wt (Fig. 5*C*), consistent with the complexome profiling findings (Fig. 5*A*), pointing out that the absence of COX6B1 allows the association of an incomplete MT-CO3 module lacking COX6A (Fig. S4*B*).

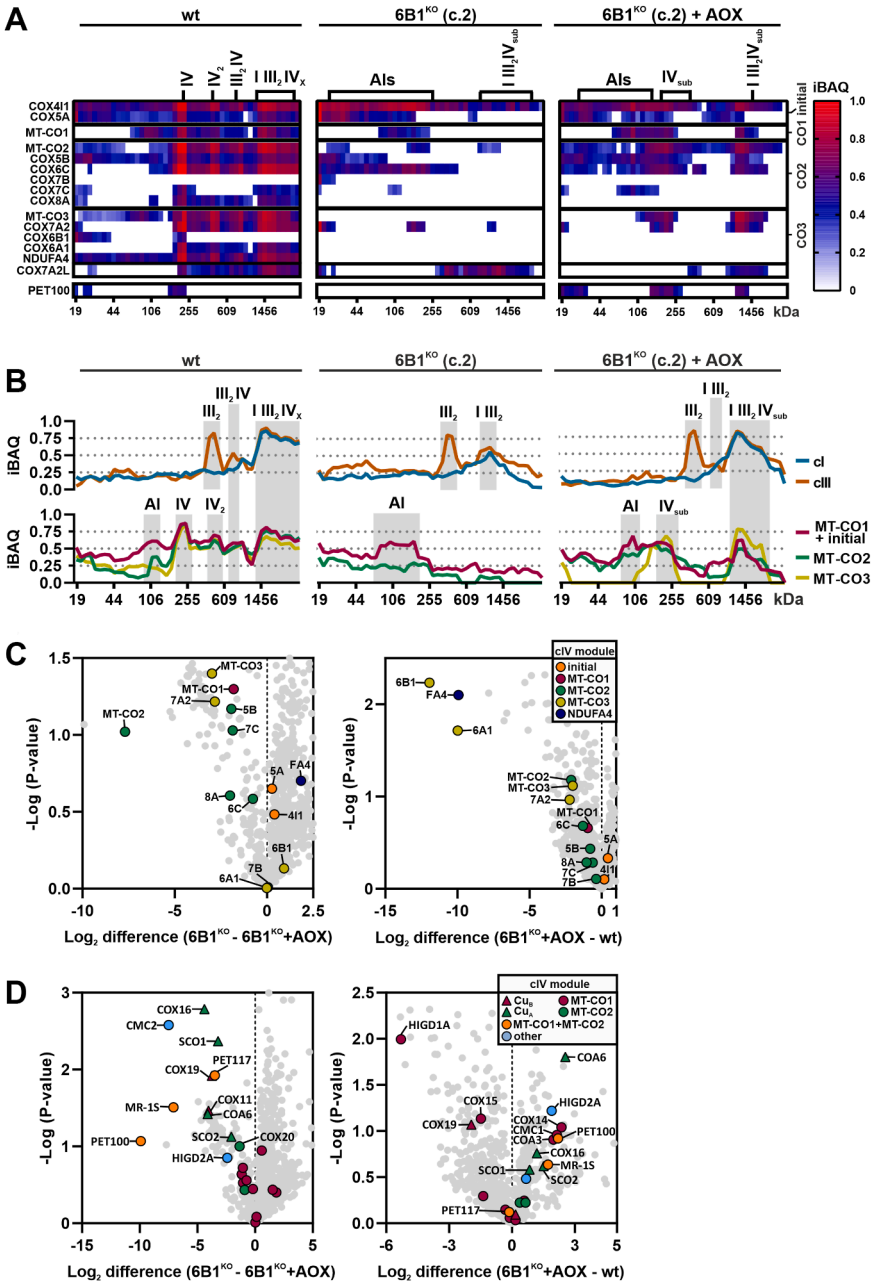

Figure 5. Expression of alternative oxidase (AOX) restores early cIV assembly block in COX6B1-deficient cells. *A*, complexome profiling analysis of cIV in wt, 6B1^{KO}, and 6B1^{KO} + AOX, respectively. Heatmap representation of relative iBAQ values of detected subunits of cIV (individual modules are marked on the *right*) and assembly factor (AF) PET100. *B*, complexome profiling analysis of cI, cIII, and cIV in wt, 6B1^{KO}, and 6B1^{KO} + AOX, respectively. XY graphs represent an average of relative iBAQ values of individual subunits of cI (*blue*) and cIII (*orange*) detected (*top*). In the case of cIV (*bottom*), the average of subunits corresponding to the individual modules (initial + MT-CO1 in *magenta*, MT-CO2 in *green*, and MT-CO3 in *yellow*) was made. In the case of the MT-CO3 module in 6B1^{KO}, no data were applied, since the MT-CO3 subunit was not detected. See also Figure S4*A*. *C*, differential amount of cIV subunits associated in cIV forms between 6B1^{KO} and 6B1^{KO} + AOX (*left*), 6B1^{KO} + AOX, and wt (*right*). Volcano plots represent LFQ–MS analysis (n = 2) of all detected proteins (*gray*) and subunits of cIV modules (initial: *orange*, MT-CO1: *magenta*, MT-CO2: *green*, MT-CO3: *yellow*, and NDUFA4: *blue*). COX6B1 protein missing in 6B1^{KO} was visualized; thanks to the imputation step (missing values replaced from a normal distribution) performed during the Perseus analysis of the LFQ–MS data. *D*, differential amount of cIV AFs associated with cIV forms between 6B1^{KO} and 6B1^{KO} + AOX (*left*), 6B1^{KO} + AOX, and wt (*right*). Volcano plots represent LFQ–MS analysis (n = 2) of all detected proteins (*gray*) and cIV assembly factors (MT-CO1 metalation: *triangle in magenta*, MT-CO1 maturation: *circle in magenta*, MT-CO2 metalation: *triangle in green*, MT-CO2 maturation: *circle in green*, MT-CO1 + MT-CO2 metalation: *triangle in yellow*, MT-CO1 + MT-CO2 association: *circle in orange*, and other: *circle in blue*). cI/III/IV, complexes I/III/IV; COX, cytochrome *c* oxidase; iBAQ, intensity-based absolute quantification; LFQ–MS, label-free quantification–mass spectrometry.

Discussion

cIV deficiency is one of the most prominent causes of mitochondrial disease (45, 46). The main genetic causes are pathogenic variants in nuclear genes encoding cIV AFs (45, 47) and, less frequently, structural subunits (8). Despite numerous studies on cIV biogenesis since the pioneering work by Nijtmans *et al.* (14), and the fact that proper cIV assembly is essential for its function and its implications for

disease, many details of cIV biogenesis remain unclear. This may be exemplified on the COX6B1 subunit, which has always been recognized as a late-stage assembling subunit (33), being a part of the MT-CO3 module (15). Consistent with this idea, skin fibroblasts and muscle biopsies from patients carrying the COX6B1 R20C variant showed an accumulation of a late cIV assembly intermediate (30). However, we have recently reported an unexpected total loss of cIV in HEK293 cell line–based COX6B1 KO ($6B1^{KO}$), similarly to what was observed in a COX4 subunit KO model, lacking the initial module of cIV assembly (21). This observation argues against the peripheral role of COX6B in the maturation of human cIV.

In order to understand the real role of the COX6B subunit for cIV assembly, we have continued to investigate in detail the molecular mechanisms underlying the severe cIV deficiency caused by the complete absence of COX6B1. Thus, $6B1^{KO}$ cells showed decreased steady-state levels of most of the cIV subunits, including the mtDNA-encoded subunit MT-CO2. This was unexpected since, according to the current cIV assembly model, MT-CO2 precedes the addition of the MT-CO3 module, to which COX6B1 belongs (15). Unlike in the KO of the COX4 subunit (21, 35), $6B1^{KO}$ still preserved the initial module subunits, COX4 and COX5A, reflected by the stabilization of assembly intermediates formed by subunits MT-CO1, COX4, and COX5A. In the $6B1^{KO}$ model, intermediates containing a residual portion of the MT-CO2 subunit were present only in trace quantities detectable by complexome profiling, and a group of cIV subunits, COX4, MT-CO2, and COX7A2 were found associated with a fully assembled SC I III_2, forming an incomplete respirasome (SC I III_2IV_{sub}). However, the assembly intermediates migrating at a slightly lower molecular weight band than cIV monomer (IV_{sub}), which would resemble the previous observation of incomplete cIV in COX6B1 patient samples (30), were not detected in $6B1^{KO}$ cells but were present when expressing the R20 COX6B1 variants. Therefore, we describe that the COX6B1 subunit is indispensable for the addition or stabilization of the MT-CO2 module in an early phase of cIV assembly. In contrast, KO models of COX7A, another subunit belonging to the MT-CO3 module, did not affect the incorporation of MT-CO2 into cIV (48). Another evidence was a decrease in the steady-state and cIV-bound levels of the AFs governing copper delivery to MT-CO2 (SCO1, SCO2, and COA6) as well as MT-CO2 module stabilization and/or binding to the MT-CO1 module (PET100) in $6B1^{KO}$. Indeed, the phenotype of $6B1^{KO}$ mirrors COA6-lacking HEK293T cells (38), since both lead toward total cIV loss. Interestingly enough, COA6 is a paralog of COX6B1 (49) and their levels seem to be interdependent (38). Likewise, pathogenic variants in PET100 were shown to diminish MT-CO2 levels in patient fibroblasts (50, 51), accompanied by a decrease in COX6B1 protein (15), leading to a total loss of fully assembled cIV (15, 51).

The process of MT-CO2 metalation, that is, Cu_A insertion, requires IMS located and redox-modulated AFs, SCO1 and SCO2 and COA6, the latter containing twin Cx9C motifs involved in the redox-mediated import, folding, and stabilization of the protein (41, 52). COX6B1 also contains Cx9C (C30/C40) and Cx10C (C54/C65) motifs (53), which by analogy to COA6 and to the yeast COX6B1 ortholog Cox12 points out to a role for COX6B1 in MT-CO2 maturation (54, 55). Strikingly, the xenoexpression of an AOX in $6B1^{KO}$ resulted in increased levels of most cIV subunits, with MT-CO2 level being the most significantly upregulated (21). The AOX overexpression has been repeatedly examined for its therapeutic potential for defects of cIII and cIV (43). Effects of AOX are complex and may counterbalance various cellular stresses (56), which can also depend on the type of AOX used (57). We hypothesize that the major effect of the AOX introduction into the context of total cIV deficiency is the restoration of electron flow from oxidized substrates to oxygen and general recovery of canonical directions of cellular metabolic pathways. This ameliorates mitochondrial redox status, and restored MT-CO2 maturation leads to stabilization of a cIV intermediate (IV_{sub}), where we detected subunits across all three cIV assembly modules. Accordingly, the factors required for coordination of the copper centers, Cu_A and Cu_B (52) were enriched within the native forms of cIV after AOX expression compared with the parental $6B1^{KO}$. In accordance, blocked MT-CO2 metalation in $6B1^{KO}$ could also be inferred by the accumulation of COX14, CMC1, and COA3 within the immunocaptured cIV, representing a complex formed together with MT-CO1 that precedes the addition of MT-CO2 (52). In addition, the most significantly increased cIV AF in $6B1^{KO}$ after AOX expression was PET100, both at the steady-state level and cIV bound, indicating enhanced association of MT-CO1 and MT-CO2 modules. Therefore, here we present the first evidence that the human COX6B1 subunit is instrumental for MT-CO2 maturation. So far, COX6B1 was related to this process only indirectly *via* a high-throughput BioID analysis of human cells using the SCO1 protein as a prey, where COX6B1 was fished out among SCO2, COA6, COX11, COX15, COX16, COX17, COX19, and COX5B (58).

Complexome profiling analysis of $6B1^{KO}$ cells expressing AOX showed that incomplete cIV assembly modules, that is, the MT-CO2 module missing COX7B, COX7C, and COX8A and the MT-CO3 module missing COX6A1 and COX6B1, assemble into SC I III_2IV_{sub}, whereas cIV_2 and SC III_2IV did not form. The absence of the cIV dimer may be explained by the proposed role of COX6B1 in cIV dimerization (59, 60). Our findings also suggest that the COX6A1 subunit is not able to join cIV in the absence of COX6B1, thus, representing the penultimate subunit of the cIV assembly process preceding the last assembling subunit NDUFA4. Despite the absence of COX6B1 and a couple of other nuclear-encoded subunits, IV_{sub} or the SC I III_2IV_{sub}, containing both MT-CO1 and MT-CO2, could theoretically provide a complete electron-transfer pathway enabling enzyme activity. Our respirometric measurements demonstrated that the present IV_{sub} may indeed have enzymatic activity, yet it remains negligible. This finding supports the claim that COX6B1 through its extensive interactions with MT-CO2 is essential

for the structure of the cytochrome *c* binding site (61). Alternatively, the impaired activity may result from incomplete maturation of the Cu_A prosthetic factor in MT-CO2 in the absence of COX6B1 because of copper relay dysfunction (55). If this was the case, it could be speculated that modulation of the redox status in $6B1^{KO}$ by AOX only allows to pass a putative MT-CO2 maturation checkpoint in cIV assembly. This also opens the possibility that in this case, COX assembly proceeds through a noncanonical pathway that does not occur under normal circumstances. Future studies in cellular models with the absence of other late-assembling subunits (COX6A and NDUFA4) should clarify these issues.

In a previous study, we reported the presence of the cI assembly intermediate without the catalytic N-module in contact with cIII dimer in COX4-lacking cells (35), indicating, also in this model, an association of partially formed individual RC complexes preceding their complete maturation. In $6B1^{KO}$, fully assembled SC I III_2 was found associated with cIV subunits COX4–COX5A (pre-I III_2IV_{sub}), consistent with the previous observations of noncanonical *de novo* assembly of cIV directly into the nascent respirasome (12, 20). In addition, PET100 was detected migrating not only with IV_{sub} but also along I III_2IV_{sub} in $6B1^{KO}$ + AOX, indicating active cIV assembly both in monomeric form and inside the respirasome. According to the present results, the addition of cIV subunits seems to be supported by the presence of an initial assembly intermediate formed by subunits MT-CO1, COX4, and COX5A, since the MT-CO1 signal was detected in the corresponding band only in $6B1^{KO}$ after AOX expression but not in 4dKO (21). However, the possibility of some species of SC I III_2IV_{sub} existing in 4dKO cells expressing AOX should be further explored, since MT-CO1 together with cIV subunits, COX5B and COX7A2, was previously detected within SC I III_2IV_{sub} in MT-CO2 lacking cells (20).

To date, the outcome of the COX6B1 pathogenic variants, R20C and R20H, was directly compared only in yeast models modeling the human variants in the *Saccharomyces cerevisiae* ortholog *COX12* (62). Nevertheless, the applicability of these findings to molecular pathological mechanisms in humans may be limited because of the differences in the cIV structure and biogenesis between yeast and humans (63). Also, despite the impairment of the respiratory growth of the *COX12* null yeast cells, Cox2p levels were still preserved at around 50% of the wt, and the introduction of R17H and R17C variants in Cox12p (analogous to R20H and R20C, respectively) did not complement the respiratory defect (62). Here, we have used novel HEK293 human cellular models with a stable expression of either R20C or R20H pathogenic variant of COX6B1 in the KO background. $6B1^{KO}$ phenotype improvement was limited in both R20C and R20H models, with partially increased respiratory rates, being mainly enhanced in the R20H model. Thus, our cellular models phenocopied findings from the original patient-based studies that presented a profoundly decreased cIV biochemical activity in fibroblasts from a patient harboring the R20H pathogenic variant, contrary to undetectable cIV activity in the case of the R20C variant. This difference also correlated with the disease presentation in patients, that is, R20H-linked encephalomyopathy (succumbed at 10 years) and R20C-linked encephalomyopathy combined with hydrocephalus and hypertrophic cardiomyopathy (succumbed at 2.5 years) (30, 31). The observed differential extent of the cIV impairment because of R20C or R20H was originally explained by a destabilization of COX6B1 interaction within cIV, which is more pronounced in the case of the R20C variant (31). However, this reasoning was based on the currently outdated structure of the bovine cIV (64), which did not contain the 14th cIV subunit NDUFA4 that is located in close proximity to R20 (65). Our findings imply that the additional Cys residue forming an artificial Cx9C motif of R20C may lead to aberrant folding and decreased content of the subunit and possibly limits the MT-CO2 maturation and thus presents as a more severe cIV aberration compared with the R20H variant. R20H variant rather destabilizes the association of COX6B1 with the complex but does not affect early cIV assembly to such an extent.

In this work, we show the dual role of the COX6B1 subunit in the assembly of cIV, refining our current understanding of the cIV assembly model (Fig. 6). Nevertheless, the exact molecular mechanism by which COX6B1 interferes with other factors like PET100 and COA6 still requires further investigation. The exact role of the Cys residues of COX6B1

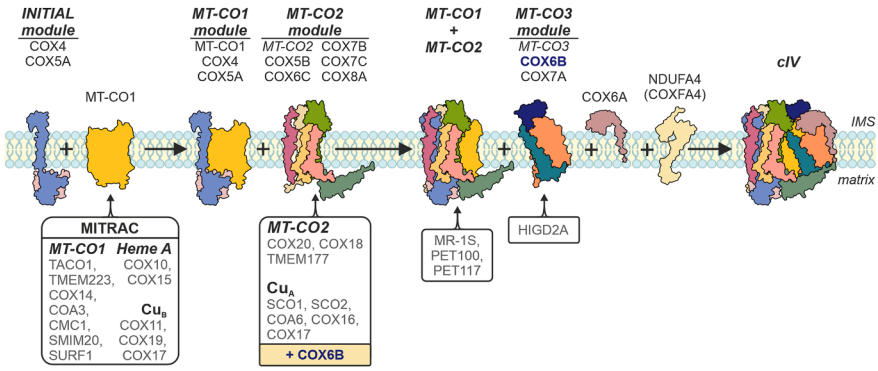

Figure 6. Updated modular model of human cIV assembly. The present scheme reflects the novel findings presented by this work. It implies COX6B subunit involvement in MT-CO2 subunit maturation. Also, the COX6A subunit incorporates at the final assembly stages independent of the MT-CO3 module. cIV, complex IV; COX, cytochrome *c* oxidase.

remains to be addressed, with an emphasis on the R20C pathogenic variant that represents a convenient model to clarify COX6B1 engagement in the MT-CO2 metalation. Also, since the COX6B2 isoform did not rescue the COX6B1-lacking HEK293 cell line, possibly for a tissue-/cell line–specific mechanism missing in these cells, its properties within the cIV biogenesis, structure, and function will require a different study model than the HEK293 cell line, that is, the spermatid cell line, sperm specimens, or animal models. Finally, the role of individual nDNA-encoded subunits in the assembly process of monomeric cIV, as well as RC SCs, should be revised in diverse KO models of cIV subunits and AFs for complete elucidation of the process, as demonstrated in this study by misconceptions of the role of COX6A and COX6B subunits.

Experimental procedures

Experimental model

HEK293 (American Type Culture Collection; CRL-1573) cells, a cell line with epithelial morphology isolated from the kidney of a human embryo, were maintained at 37 °C and 5% CO_2 atmosphere in Dulbecco's modified Eagle's medium/F-12 medium (Biowest; catalog no.: L0092) supplemented with 10% (v/v) fetal bovine serum (Thermo Fisher Scientific; catalog no.: 10270-106), 40 mM Hepes, antibiotics (100 U/ml penicillin + 100 μg/ml streptomycin; Thermo Fisher Scientific, catalog no.: 15140-122), and 50 μM uridine.

Experimental procedure details

Generation of HEK293 cellular models

COX6B1 HEK293 (American Type Culture Collection; CRL-1573) KO cells ($6B1^{KO}$, clone 1—c.1, 2—c.2, and 3—c.3) were generated previously (21). For AOX expression in $6B1^{KO}$ (c.1 and c.2) cells (to produce $6B1^{KO}$ + AOX), pcDNA3.1+ mammalian expression vector (Thermo Fisher Scientific) containing the coding sequence of full-length AOX (from *Aspergillus nidulans*), followed by a C-terminal HA-tag (66), was transfected using Metafectene Pro (Biontex Laboratories GmbH). For COX6B1 and COX6B2 expression in $6B1^{KO}$ (c.2) cells, pcDNA3.1^{+} mammalian expression vector (Thermo Fisher Scientific) containing the coding sequence of full-length human COX6B1 or COX6B2 protein followed by a C-terminal FLAG-tag (to produce $6B1^{KO}$ + 6B1, and $6B1^{KO}$ + $6B2^{C\text{-}FLAG}$, respectively), or an N-terminal FLAG-tag in the case of COX6B2 (to produce $6B1^{KO}$ + $6B2^{N\text{-}FLAG}$), was transfected using Metafectene Pro. The pcDNA3.1^{+} construct with a C-terminal FLAG-tagged COX6B1 was used to introduce mutations, leading to single amino acid substitutions of arginine residue at position 20 (COX6B1-R20) to mimic two pathogenic variants of COX6B1 found in patients (30, 31), either to cysteine (R20C) or histidine (R20H). Mutations were introduced by the QuikChange Lightning kit (Agilent), using primers (see key resources table) suggested by the manufacturer's online primer design tool. Mutagenesis was confirmed by sequencing, and mutated constructs were used for knock-in into $6B1^{KO}$ (c.2) cells to produce $6B1^{KO}$ + R20C and $6B1^{KO}$ + R20H models. Stably transfected cells were selected with 2 mg/ml G418.

SDS-PAGE

Protein separation under denaturing conditions was performed using tricine–SDS-PAGE. Protein samples were prepared from frozen cellular pellets as described (67, 68). Proteins (20 to 30 μg) were separated on 12% polyacrylamide gels using the Mini-PROTEAN III apparatus (Bio-Rad). Experiments were performed at least three times to assess the statistical significance of the results.

Native and 2D electrophoresis

For the separation of native protein complexes, BN-PAGE (69) was performed. For 2D (BN/SDS)-PAGE and complexome profiling, mitochondrial pellets were isolated from freshly harvested cells by hypotonic shock followed by differential centrifugation (70) and solubilized using the mild detergent digitonin (6 g detergent/1 g protein) to preserve SC association. Final samples (30 μg protein) (68, 69) were separated on a 4% to 13% polyacrylamide gradient gel using the Mini-PROTEAN III apparatus. Afterward, gel was cut into single lanes and either used for complexome profiling analysis or for a second dimension of 2D electrophoresis (SDS-PAGE) after 1 h incubation in dissociation solution (1% SDS and 1% 2-mercaptoethanol).

For BN-PAGE separation (Fig. S4*B*), the mitochondrial-enriched fraction was obtained by digitonin treatment of the freshly harvested cellular pellets, which was further solubilized by *n*-dodecyl-β-D-maltoside based on the protocol (71). Samples were separated on a precast commercial native gel (NativePAGE 3%–12% Bis–Tris Gels; Thermo Fisher Scientific, catalog no.: BN1001BOX) as described (71).

WB and immunodetection

Proteins separated by SDS-PAGE were transferred to polyvinylidene difluoride membranes (Immobilon FL 0.45 μm; Merck) by semidry electroblotting (0.8 mA/cm^2, 1 h) using a Transblot SD apparatus (Bio-Rad). BN-PAGE gels were transferred to polyvinylidene difluoride membranes using Dunn's carbonate buffer (10 mM $NaHCO_3$, 3 mM $Na2CO_3$), applying a constant voltage of 100 V at 4 °C for 1 h using a Mini Trans-Blot Cell (Bio-Rad). Immunodetection was performed as described (68), using validated primary (see supporting information 2—Validation information on antibodies) and fluorescent secondary antibodies listed in the Key resources table, finally detected by the fluorescence scanner Odyssey (LI-COR Biosciences). The resulting signals were analyzed and quantified by Image Lab software (Bio-Rad).

LFQ–MS analysis

Proteomic analysis was performed by the Proteomics Service Laboratory at the Institute of Physiology and the Institute of Molecular Genetics of the Czech Academy of Sciences. LFQ–MS of cell pellets was performed. Briefly, cellular pellets

(100 μg of protein) were processed according to the protocol for in-solution trypsin digestion (35). About 1 μg of peptide digests were separated on a 50 cm C18 column using 2.5 h gradient elution and analyzed in a data-dependent acquisition mode on the Orbitrap Exploris 480 (Thermo Fisher Scientific) mass spectrometer. The resulting raw files were processed in MaxQuant (version 1.5.3.28, maxquant.org) (72) with the LFQ algorithm MaxLFQ (73). Imputation of missing values was performed in Perseus (http://www.perseus-framework.org) using default values (replaced from a normal distribution, width 0.3, down shift 1.8). LFQ–MS data are available *via* ProteomeXchange with identifier PXD061621.

Immunoprecipitation and MS analysis

Mitochondrial membranes solubilized with digitonin (6 g/g of protein) were immunoprecipitated using the cIV immunocapture kit (Abcam; catalog no.: ab109801). Proteomic analysis was performed by the Proteomics Service Laboratory at the Institute of Physiology and the Institute of Molecular Genetics of the Czech Academy of Sciences. Washed beads with immunocaptured complexes were digested "on beads" with trypsin using the sodium deoxycholate procedure as described (74). Desalted peptide digests were separated on a 50 cm C18 column using a 1 h elution gradient and were analyzed on Orbitrap Exploris 480 MS. Resulting raw files were processed in MaxQuant (version 1.6.6.0) with the LFQ algorithm MaxLFQ (73). Analysis was performed in duplicate. Imputation of missing values was performed in Perseus using default values (replaced from normal distribution, width 0.3, and down shift 1.8). LFQ–MS data are available *via* ProteomeXchange with identifier PXD061621.

Complexome profiling

Isolated mitochondria from wt, $6B1^{KO}$, and $6B1^{KO}$ + AOX cells were solubilized by digitonin (6 g detergent/1 g protein), and samples for BN-PAGE separation were prepared as described earlier. Finalized samples (50 μg) were subjected to 4% to 13% polyacrylamide gradient gel using the Mini-PROTEAN III apparatus. The gel was fixed (1 methanol:1 dH_2O; 5% acetic acid), washed in dH_2O, and excised in 48 slices. Slices were cut to 1 mm^3 cubes and transferred to a 96-well filter plate (Multiscreen Solvinert MSRLN0450, 0.45 μm pore size PTFE membrane; Merck Millipore). Proteomic analysis was performed by the Proteomics Service Laboratory at the Institute of Physiology and the Institute of Molecular Genetics of the Czech Academy of Sciences. In-gel digestion was performed according to the protocol (75) modified for a 96-well filter plate processed on a vacuum manifold. Briefly, reduction by DTT was followed by iodoacetamide alkylation, destaining, and trypsin digestion. Tryptic peptides were extracted, dried, dissolved, desalted by one-layer C18 StageTips, and transferred to a U-shaped 96-well plate suitable for the Ultimate 3000 Nano UHPLC autosampler. Peptides were separated on a 15 cm C18 column using 30 min elution gradient and analyzed in a data-dependent acquisition mode on Orbitrap Exploris 480 MS. Raw files were processed in MaxQuant (version 1.6.17.0). The intensity-based absolute quantification values of each protein detected in the individual slices were normalized to the protein with the highest intensity and were visualized in the heatmaps using Microsoft Excel and Prism 8 (GraphPad Software). Complexome profiling data are available *via* ProteomeXchange with identifier PXD061618.

High-resolution respirometry

Mitochondrial respiration was measured at 37 °C as described (76) using Oxygraph-2k (Oroboros), essentially as described (77). Freshly harvested cells (0.4–1.5 mg of protein) were suspended in 2 ml of MiR05 medium (0.5 mM EGTA, 3 mM $MgCl_2$, 60 mM lactobionic acid, 20 mM taurine, 10 mM KH_2PO_4, 20 mM Hepes, 110 mM D-sucrose, and 1 g/l of bovine serum albumin, pH 7.1) (78), and digitonin (0.05 g/g protein) was used to permeabilize the plasma membrane. For measurements, the following substrates and inhibitors were used: 2 mM malate, 10 mM pyruvate, 10 mM glutamate, 10 mM succinate, 10 mM glycerol 3-phosphate, 1 mM ADP, 0.5 μM oligomycin, 0.5 to 2 μM FCCP, 0.5 μM rotenone, 10 mM malonate, 0.25 μM antimycin A, 2 mM ascorbate, 1 mM TMPD, 0.5 mM KCN, 0.5 mM salicylhydroxamic acid (inhibitor of AOX). The oxygen consumption was expressed in pmol O_2/s/mg protein. Data were acquired and analyzed using routine functions of Datlab 5 software (Oroboros). Representative trace of the respiratory protocol is shown in Figure S1*E*. Three respiratory states were chosen for data reporting: (i) OXPHOS—actively phosphorylating cells supplied fully saturated with substrates (pyruvate, glutamate, malate, succinate, and glycerol 3-phosphate) and ADP, (ii) ETS—maximal respiratory capacity of the ETS (fully saturated with substrates, after FCCP uncoupling), (iii) COX—oxygen consumption by COX fueled by artificial substrates ascorbate + TMPD, corrected for KCN-insensitive background oxygen consumption).

Data analysis, visualization, and statistics

Data were analyzed and visualized in GraphPad Prism 8 software (GraphPad Software), including normality and outliers testing. Downstream analysis of LFQ–MS data was performed in Perseus (versions 2.3.0.0 and 2.0.11.0) (72) and data were further visualized in GraphPad Prism 8. One-way ANOVA (*asterisks* represent p value: *<0.05; **<0.01; and ***<0.001) was used. Significant changes between individual samples and wt are represented by a symbol over the corresponding bar, whereas comparison between other models is indicated by a star symbol on top of a connecting line. Data shown in the graphs represent the mean values ± SD of at least three independent experiments, n indicates the number of biological replicates.

The key resource table is attached as an individual supporting information file.

Resource availability

Lead contact

Further information and requests for resources and reagents should be directed to and will be fulfilled by the lead contact, Petr Pecina (petr.pecina@fgu.cas.cz).

Material availability

- This study did not generate new unique reagents.

Data and code availability

- The MS proteomics data from the LFQ analysis have been deposited to the ProteomeXchange Consortium *via* the PRIDE (79) partner repository with the dataset identifier PXD061621.
- The MS proteomics data from the complexome profiling analysis have been deposited to the ProteomeXchange Consortium *via* the PRIDE (79) partner repository with the dataset identifier PXD061618.
- Original WB images reported in this article will be shared by the lead contact upon request.
- Any additional information required to reanalyze the data reported in this article is available from the lead contact upon request.
- This article does not report original code.

Supporting information—This article contains supporting information.

Acknowledgments—We acknowledge the Proteomics Service Laboratory at the Institute of Physiology (supported by RVO, ID 67985823) and the Institute of Molecular Genetics (supported by RVO, ID 68378050) of the Czech Academy of Sciences.

Author contributions—K. Č., M. V., and P. P. conceptualization; K. Č., M. V., and P. P. methodology; K. Č., M. V., M. K., A. P., and P.P. investigation; K. Č. and P.P. writing–original draft; K. Č., A. P., L. A., J. H., E. F.-V., T. M., and P. P. writing–review & editing; K. Č. visualization; T. M. and P. P. supervision; T. M. and P. P. project administration; J. H. and P. P. funding acquisition.

Funding and additional information—This research was supported by Czech Science Foundation projects (22-21082S and 22-21552S), Czech Health Research Council (NU22-01-00499), and by the National Institute for Research of Metabolicand Cardiovascular Diseases (Program EXCELES, ID Project No.LX22NPO5104) funded by the European Union—Next Generation EU. K. Č. is the recipient of an EMBO Postdoctoral Fellowship (grant no.: ALTF 710-2022).

Conflict of interest—The authors declare that they have no conflicts of interest with the contents of this article.

Abbreviations—The abbreviations used are: AF, assembly factor; AOX, alternative oxidase; BN-PAGE, Blue Native PAGE; CI/III/IV, complexes I/III/IV; COX, cytochrome c oxidase; ETS, electron transporting system; HEK293, human embryonic kidney 293 cell line; IMS, intermembrane space; KCN, potassium cyanide; LFQ–MS, label-free quantification–mass spectrometry; MS, mass spectrometry; mtDNA, mitochondrial DNA; nDNA, nuclear DNA; OXPHOS, oxidative phosphorylation; RC, respiratory chain; SC, supercomplex; TMPD, tetramethylphenylenediamine; WB, Western blot.

References

1. Villani, G., and Attardi, G. (2000) In vivo control of respiration by cytochrome c oxidase in human cells. *Free Radic. Biol. Med.* **29**, 202–210
2. Schagger, H., and Pfeiffer, K. (2000) Supercomplexes in the respiratory chains of yeast and mammalian mitochondria. *EMBO J.* **19**, 1777–1783
3. Kadenbach, B., and Merle, P. (1981) On the function of multiple subunits of cytochrome c oxidase from higher eukaryotes. *FEBS Lett.* **135**, 1–11
4. Tsukihara, T., Aoyama, H., Yamashita, E., Tomizaki, T., Yamaguchi, H., Shinzawa-Itoh, K., *et al.* (1996) The whole structure of the 13-subunit oxidized cytochrome c oxidase at 2.8 A. *Science* **272**, 1136–1144
5. Pitceathly, R. D. S., and Taanman, J.-W. (2018) NDUFA4 (Renamed COXFA4) is a Cytochrome-c oxidase subunit. *Trends Endocrinol. Metab.* **29**, 452–454
6. Blomme, T., Vandepoele, K., De Bodt, S., Simillion, C., Maere, S., and Van de Peer, Y. (2006) The gain and loss of genes during 600 million years of vertebrate evolution. *Genome Biol.* **7**, R43
7. Little, A. G., Kocha, K. M., Lougheed, S. C., and Moyes, C. D. (2010) Evolution of the nuclear-encoded cytochrome oxidase subunits in vertebrates. *Physiol. Genomics* **42**, 76–84
8. Čunátova, K., Reguera, D. P., Houštěk, J., Mráček, T., and Pecina, P. (2020) Role of cytochrome c oxidase nuclear-encoded subunits in health and disease. *Physiol. Res.* **69**, 947–965
9. Vogt, S., Ramzan, R., Grossman, L. I., Singh, K. K., Ferguson-Miller, S., Yoshikawa, S., *et al.* (2021) Mitochondrial respiration is controlled by Allostery, subunit composition and phosphorylation sites of cytochrome c oxidase: a trailblazer's tale - bernhard Kadenbach. *Mitochondrion* **60**, 228–233
10. Ikeda, K., Shiba, S., Horie-Inoue, K., Shimokata, K., and Inoue, S. (2013) A stabilizing factor for mitochondrial respiratory supercomplex assembly regulates energy metabolism in muscle. *Nat. Commun.* **4**, 2147
11. Lapuente-Brun, E., Moreno-Loshuertos, R., Acin-Perez, R., Latorre-Pellicer, A., Colas, C., Balsa, E., *et al.* (2013) Supercomplex assembly determines electron flux in the mitochondrial electron transport chain. *Science* **340**, 1567–1570
12. Timon-Gomez, A., Garlich, J., Stuart, R. A., Ugalde, C., and Barrientos, A. (2020) Distinct roles of mitochondrial HIGD1A and HIGD2A in respiratory complex and Supercomplex biogenesis. *Cell Rep.* **31**, 107607
13. Vercellino, I., and Sazanov, L. A. (2021) Structure and assembly of the mammalian mitochondrial supercomplex CIII2CIV. *Nature* **598**, 364–367
14. Nijtmans, L. G., Taanman, J. W., Muijsers, A. O., Speijer, D., and Van den Bogert, C. (1998) Assembly of cytochrome-c oxidase in cultured human cells. *Eur. J. Biochem.* **254**, 389–394
15. Vidoni, S., Harbour, M. E., Guerrero-Castillo, S., Signes, A., Ding, S., Fearnley, I. M., *et al.* (2017) MR-1S interacts with PET100 and PET117 in module-based assembly of human cytochrome c oxidase. *Cell Rep.* **18**, 1727–1738
16. Signes, A., and Fernandez-Vizarra, E. (2018) Assembly of mammalian oxidative phosphorylation complexes I–V and supercomplexes. *Essays Biochem.* **62**, 255–270
17. Timón-Gómez, A., Nývltová, E., Abriata, L. A., Vila, A. J., Hosler, J., and Barrientos, A. (2018) Mitochondrial cytochrome c oxidase biogenesis: recent developments. *Semin. Cell Dev Biol* **76**, 163–178
18. Lazarou, M., Smith, S. M., Thorburn, D. R., Ryan, M. T., and McKenzie, M. (2009) Assembly of nuclear DNA-encoded subunits into mitochondrial complex IV, and their preferential integration into supercomplex forms in patient mitochondria. *FEBS J.* **276**, 6701–6713
19. Moreno-Lastres, D., Fontanesi, F., Garcia-Consuegra, I., Martin, M. A., Arenas, J., Barrientos, A., *et al.* (2012) Mitochondrial complex I plays an essential role in human respirasome assembly. *Cell Metab* **15**, 324–335

20. Lobo-Jarne, T., Perez-Perez, R., Fontanesi, F., Timon-Gomez, A., Wittig, I., Penas, A., *et al.* (2020) Multiple pathways coordinate assembly of human mitochondrial complex IV and stabilization of respiratory supercomplexes. *EMBO J.* **39**, e103912
21. Čunátová, K., Vrbacký, M., Puertas-Frias, G., Alán, L., Vanišová, M., Saucedo-Rodríguez, M. J., *et al.* (2024) Mitochondrial translation is the primary determinant of secondary mitochondrial complex I deficiencies. *iScience* **27**, 110560
22. Tang, J. X., Cabrera-Orefice, A., Meisterknecht, J., Taylor, L. S., Monteuuis, G., Stensland, M. E., *et al.* (2025) COA5 has an essential role in the early stage of mitochondrial complex IV assembly. *Life Sci. Alliance* **8**, e202403013
23. Fernández-Vizarra, E., and Ugalde, C. (2022) Cooperative assembly of the mitochondrial respiratory chain. *Trends Biochem. Sci.* **47**, 999–1008
24. Hüttemann, M., Jaradat, S., and Grossman, L. I. (2003) Cytochrome c oxidase of mammals contains a testes-specific isoform of subunit VIb — the counterpart to testes-specific cytochrome c. *Mol. Reprod. Dev.* **66**, 8–16
25. Cao, X., Cui, Y., Zhang, X., Lou, J., Zhou, J., Bei, H., *et al.* (2018) Proteomic profile of human spermatozoa in healthy and asthenozoospermic individuals. *Reprod. Biol. Endocrinol.* **16**, 4–11
26. Shimada, K., Lu, Y., and Ikawa, M. (2024) Disruption of testis-enriched cytochrome c oxidase subunit COX6B2 but not COX8C leads to subfertility. *Exp. Anim.* **73**, 1–10
27. Maxfield, K. E., Taus, P. J., Corcoran, K., Wooten, J., Macion, J., Zhou, Y., *et al.* (2015) Comprehensive functional characterization of cancer-testis antigens defines obligate participation in multiple hallmarks of cancer. *Nat. Commun.* **6**, 8840
28. Cheng, C. C., Wooten, J., Gibbs, Z. A., McGlynn, K., Mishra, P., and Whitehurst, A. W. (2020) Sperm-specific COX6B2 enhances oxidative phosphorylation, proliferation, and survival in human lung adenocarcinoma. *Elife* **9**, e58108
29. Nie, K., Li, J., He, X., Wang, Y., Zhao, Q., Du, M., *et al.* (2020) COX6B2 drives metabolic reprogramming toward oxidative phosphorylation to promote metastasis in pancreatic ductal cancer cells. *Oncogenesis* **9**, 51
30. Massa, V., Fernández-Vizarra, E., Alshahwan, S., Bakhsh, E., Goffrini, P., Ferrero, I., *et al.* (2008) Severe infantile encephalomyopathy caused by a mutation in COX6B1 , a nucleus-encoded subunit of cytochrome C oxidase. *Am. J. Hum. Genet.* **82**, 1281–1289
31. Abdulhag, U. N., Soiferman, D., Schueler-Furman, O., Miller, C., Shaag, A., Elpeleg, O., *et al.* (2015) Mitochondrial complex IV deficiency, caused by mutated COX6B1, is associated with encephalomyopathy, hydrocephalus and cardiomyopathy. *Eur. J. Hum. Genet.* **23**, 159–164
32. Jennions, E., Olsson-Engman, M., Visuttijai, K., Wiksell, Å., Fluriach Dominguez, N., Kollberg, G., *et al.* (2024) A novel homozygous pathogenic missense variant in COX6B1: further delineation of the phenotype. *Am. J. Med. Genet. A.* **194**, e63783
33. Fornůsková, D., Stibůrek, L., Wenchich, L., Vinsova, K., Hansíková, H., and Zeman, J. (2010) Novel insights into the assembly and function of human nuclear-encoded cytochrome c oxidase subunits 4, 5a, 6a, 7a and 7b. *Biochem. J.* **428**, 363–374
34. Hock, D. H., Reljic, B., Ang, C. S., Muellner-Wong, L., Mountford, H. S., Compton, A. G., *et al.* (2020) HIGD2A is required for assembly of the COX3 module of human mitochondrial complex IV. *Mol. Cell Proteomics* **19**, 1145–1160
35. Čunátová, K., Reguera, D. P., Vrbacký, M., Fernández-Vizarra, E., Ding, S., Fearnley, I. M., *et al.* (2021) Loss of COX4I1 leads to combined respiratory chain deficiency and impaired mitochondrial protein synthesis. *Cells* **10**, 369
36. Zarges, C., and Riemer, J. (2024) Oxidative protein folding in the intermembrane space of human mitochondria. *FEBS Open Bio* **14**, 1610–1626
37. Pacheu-Grau, D., Bareth, B., Dudek, J., Juris, L., Vögtle, F. N., Wissel, M., *et al.* (2015) Cooperation between COA6 and SCO2 in COX2 maturation during cytochrome c oxidase assembly links two mitochondrial cardiomyopathies. *Cell Metab.* **21**, 823–833
38. Stroud, D. A., Maher, M. J., Lindau, C., Vögtle, F.-N., Frazier, A. E., Surgenor, E., *et al.* (2015) COA6 is a mitochondrial complex IV assembly factor critical for biogenesis of mtDNA-encoded COX2. *Hum. Mol. Genet.* **24**, 5404–5415
39. Soma, S., Morgada, M. N., Naik, M. T., Boulet, A., Roesler, A. A., Dziuba, N., *et al.* (2019) COA6 is structurally tuned to function as a thiol-disulfide oxidoreductase in copper delivery to mitochondrial cytochrome c oxidase. *Cell Rep.* **29**, 4114–4126.e4115
40. Bourens, M., Fontanesi, F., Soto, I. C., Liu, J., and Barrientos, A. (2013) Redox and reactive oxygen species regulation of mitochondrial cytochrome C oxidase biogenesis. *Antioxid. Redox Signal* **19**, 1940–1952
41. Povea-Cabello, S., Brischigliaro, M., and Fernández-Vizarra, E. (2024) Emerging mechanisms in the redox regulation of mitochondrial cytochrome c oxidase assembly and function. *Biochem. Soc. Trans.* **52**, 873–885
42. Young, L., Shiba, T., Harada, S., Kita, K., Albury, M. S., and Moore, A. L. (2013) The alternative oxidases: simple oxidoreductase proteins with complex functions. *Biochem. Soc. Trans.* **41**, 1305–1311
43. Viscomi, C., Moore, A. L., Zeviani, M., and Szibor, M. (2023) Xenotopic expression of alternative oxidase (AOX) to study mechanisms of mitochondrial disease. *Biochim. Biophys. Acta Bioenerg.* **1864**, 148947
44. Cabrera-Orefice, A., Potter, A., Evers, F., Hevler, J. F., and Guerrero-Castillo, S. (2022) Complexome profiling—exploring mitochondrial protein complexes in health and disease. *Front. Cell Dev. Biol.* **9**, 796128
45. Fernandez-Vizarra, E., and Zeviani, M. (2021) Mitochondrial disorders of the OXPHOS system. *FEBS Lett.* **595**, 1062–1106
46. Gorman, G. S., Chinnery, P. F., DiMauro, S., Hirano, M., Koga, Y., McFarland, R., *et al.* (2016) Mitochondrial diseases. *Nat. Rev. Dis. Primers* **2**, 16080
47. Pecina, P., Gnaiger, E., Zeman, J., Pronicka, E., and Houstek, J. (2004) Decreased affinity for oxygen of cytochrome-c oxidase in leigh syndrome caused by SURF1 mutations. *Am. J. Physiol. Cell Physiol.* **287**, C1384–C1388
48. Fernández-Vizarra, E., López-Calcerrada, S., Sierra-Magro, A., Pérez-Pérez, R., Formosa, L. E., Hock, D. H., *et al.* (2022) Two independent respiratory chains adapt OXPHOS performance to glycolytic switch. *Cell Metab.* **34**, 1792–1808.e1796
49. Szklarczyk, R., Wanschers, B. F., Cuypers, T. D., Esseling, J. J., Riemersma, M., van den Brand, M. A., *et al.* (2012) Iterative orthology prediction uncovers new mitochondrial proteins and identifies C12orf62 as the human ortholog of COX14, a protein involved in the assembly of cytochrome c oxidase. *Genome Biol.* **13**, R12
50. Oláhová, M., Haack, T. B., Alston, C. L., Houghton, J. A., He, L., Morris, A. A., *et al.* (2015) A truncating PET100 variant causing fatal infantile lactic acidosis and isolated cytochrome c oxidase deficiency. *Eur. J. Hum. Genet.* **23**, 935–939
51. Lim, S. C., Smith, K. R., Stroud, D. A., Compton, A. G., Tucker, E. J., Dasvarma, A., *et al.* (2014) A founder mutation in PET100 causes isolated complex IV deficiency in Lebanese individuals with leigh syndrome. *Am. J. Hum. Genet.* **94**, 209–222
52. Nývltová, E., Dietz, J. V., Seravalli, J., Khalimonchuk, O., and Barrientos, A. (2022) Coordination of metal center biogenesis in human cytochrome c oxidase. *Nat. Commun.* **13**, 3615
53. Gladyck, S., Aras, S., Hüttemann, M., and Grossman, L. I. (2021) Regulation of COX assembly and function by twin CX9C proteins—implications for human disease. *Cells* **10**, 197
54. Nieto-Panqueva, F., Vázquez-Acevedo, M., Barrera-Gómez, D. F., Gavilanes-Ruiz, M., Hamel, P. P., and González-Halphen, D. (2024) A high copy suppressor screen identifies factors enhancing the allotopic production of subunit II of cytochrome c oxidase. *G3 (Bethesda)* **15**, jkae295
55. Ghosh, A., Pratt, A. T., Soma, S., Theriault, S. G., Griffin, A. T., Trivedi, P. P., *et al.* (2016) Mitochondrial disease genes COA6, COX6B and SCO2 have overlapping roles in COX2 biogenesis. *Hum. Mol. Genet.* **25**, 660–671
56. Jacobs, H. T., and Ballard, J. W. O. (2022) What physiological role(s) does the alternative oxidase perform in animals? *Biochim. Biophys. Acta Bioenerg.* **1863**, 148556
57. Hernansanz-Agustin, P., and Enriquez, J. A. (2023) Alternative respiratory oxidases to study the animal electron transport chain. *Biochim. Biophys. Acta Bioenerg.* **1864**, 148936

58. Antonicka, H., Lin, Z.-Y., Janer, A., Aaltonen, M. J., Weraarpachai, W., Gingras, A.-C., *et al.* (2020) A high-density human mitochondrial proximity interaction network. *Cell Metab.* **32**, 479–497.e479
59. Weishaupt, A., and Kadenbach, B. (1992) Selective removal of subunit VIb increases the activity of cytochrome c oxidase. *Biochemistry* **31**, 11477–11481
60. Kadenbach, B., and Hüttemann, M. (2015) The subunit composition and function of mammalian cytochrome c oxidase. *Mitochondrion* **24**, 64–76
61. Shimada, S., Shinzawa-Itoh, K., Baba, J., Aoe, S., Shimada, A., Yamashita, E., *et al.* (2017) Complex structure of cytochrome c-cytochrome c oxidase reveals a novel protein-protein interaction mode. *Embo j* **36**, 291–300
62. Das, S., Mukherjee, S., Bedi, M., and Ghosh, A. (2021) Mutations in the yeast Cox12 subunit severely compromise the activity of the mitochondrial complex IV. *Biochemistry (Moscow)* **86**, 1607–1623
63. Caron-Godon, C. A., Collington, E., Wolf, J. L., Coletta, G., and Glerum, D. M. (2024) More than just bread and wine: using yeast to understand inherited cytochrome oxidase deficiencies in humans. *Int. J. Mol. Sci.* **25**, 3814
64. Muramoto, K., Hirata, K., Shinzawa-Itoh, K., Yoko-o, S., Yamashita, E., Aoyama, H., *et al.* (2007) A histidine residue acting as a controlling site for dioxygen reduction and proton pumping by cytochrome *c* oxidase. *Proc. Natl. Acad. Sci. U. S. A.* **104**, 7881–7886
65. Zong, S., Wu, M., Gu, J., Liu, T., Guo, R., and Yang, M. (2018) Structure of the intact 14-subunit human cytochrome c oxidase. *Cell Res.* **28**, 1026–1034
66. Perales-Clemente, E., Bayona-Bafaluy, M. P., Pérez-Martos, A., Barrientos, A., Fernández-Silva, P., and Enriquez, J. A. (2008) Restoration of electron transport without proton pumping in mammalian mitochondria. *Proc. Natl. Acad. Sci. U. S. A.* **105**, 18735–18739
67. Schägger, H. (2006) Tricine–SDS-PAGE. *Nat. Protoc.* **1**, 16–22
68. Pajuelo Reguera, D., Cunatova, K., Vrbacky, M., Pecinova, A., Houstek, J., Mracek, T., *et al.* (2020) Cytochrome c oxidase subunit 4 isoform exchange results in modulation of oxygen affinity. *Cells* **9**, 443
69. Wittig, I., Braun, H.-P., and Schägger, H. (2006) Blue native PAGE. *Nat. Protoc.* **1**, 418–428
70. Bentlage, H. A. C. M., Wendel, U., Schagger, H., ter Laak, H. J., Janssen, A. J. M., and Trijbels, J. M. F. (1996) Lethal infantile mitochondrial disease with isolated complex I deficiency in fibroblasts but with combined complex I and IV deficiencies in muscle. *Neurology* **47**, 243–248
71. Fernandez-Vizarra, E., and Zeviani, M. (2021) Blue-native electrophoresis to study the OXPHOS complexes. *Methods Mol. Biol.* **2192**, 287–311
72. Tyanova, S., Temu, T., and Cox, J. (2016) The MaxQuant computational platform for mass spectrometry-based shotgun proteomics. *Nat. Protoc.* **11**, 2301–2319
73. Cox, J., Hein, M. Y., Luber, C. A., Paron, I., Nagaraj, N., and Mann, M. (2014) Accurate proteome-wide label-free quantification by delayed normalization and maximal peptide ratio extraction, termed MaxLFQ. *Mol. Cell. Proteomics* **13**, 2513–2526
74. Hartmannová, H., Piherová, L., Tauchmannová, K., Kidd, K., Acott, P. D., Crocker, J. F., *et al.* (2016) Acadian variant of Fanconi syndrome is caused by mitochondrial respiratory chain complex I deficiency due to a non-coding mutation in complex I assembly factor NDUFAF6. *Hum. Mol. Genet.* **25**, 4062–4079
75. Shevchenko, A., Tomas, H., Havli, J., Olsen, J. V., and Mann, M. (2006) In-gel digestion for mass spectrometric characterization of proteins and proteomes. *Nat. Protoc.* **1**, 2856–2860
76. Pecina, P., Houšťková, H., Mráček, T., Pecinová, A., Nůsková, H., Tesařová, M., *et al.* (2014) Noninvasive diagnostics of mitochondrial disorders in isolated lymphocytes with high resolution respirometry. *BBA Clin.* **2**, 62–71
77. Korandová, Z., Pecina, P., Pecinová, A., Koňaříková, E., Tesařová, M., Houštěk, J., *et al.* (2025) Cryopreserved PBMCs can be used for the analysis of mitochondrial respiration and serve as a diagnostic tool for mitochondrial diseases. *Anal Biochem.* **698**, 115745
78. Komlódi, T., Sobotka, O., Krumschnabel, G., Bezuidenhout, N., Hiller, E., Doerrier, C., *et al.* (2018) Comparison of mitochondrial incubation media for measurement of respiration and hydrogen peroxide production. *Methods Mol. Biol.* **1782**, 137–155
79. Perez-Riverol, Y., Bandla, C., Kundu, D. J., Kamatchinathan, S., Bai, J., Hewapathirana, S., *et al.* (2025) The PRIDE database at 20 years: 2025 update. *Nucleic Acids Res.* **53**, D543–d553
80. Mick, D. U., Dennerlein, S., Wiese, H., Reinhold, R., Pacheu-Grau, D., Lorenzi, I., *et al.* (2012) MITRAC links mitochondrial protein translocation to respiratory-chain assembly and translational regulation. *Cell* **151**, 1528–1541
81. Dennerlein, S., and Rehling, P. (2015) Human mitochondrial COX1 assembly into cytochrome c oxidase at a glance. *J. Cell Sci.* **128**, 833–837
82. Stiburek, L., Vesela, K., Hansikova, H., Pecina, P., Tesarova, M., Cerna, L., *et al.* (2005) Tissue-specific cytochrome c oxidase assembly defects due to mutations in SCO2 and SURF1. *Biochem. J.* **392**, 625–632
83. Aich, A., Wang, C., Chowdhury, A., Ronsor, C., Pacheu-Grau, D., Richter-Dennerlein, R., *et al.* (2018) COX16 promotes COX2 metallation and assembly during respiratory complex IV biogenesis. *Elife* **7**, e32572
84. Maghool, S., Cooray, N. D. G., Stroud, D. A., Aragao, D., Ryan, M. T., and Maher, M. J. (2019) Structural and functional characterization of the mitochondrial complex IV assembly factor Coa6. *Life Sci. Alliance* **2**, e201900458
85. Pacheu-Grau, D., Wasilewski, M., Oeljeklaus, S., Gibhardt, C. S., Aich, A., Chudenkova, M., *et al.* (2020) COA6 facilitates cytochrome c oxidase biogenesis as thiol-reductase for copper metallochaperones in Mitochondria. *J. Mol. Biol.* **432**, 2067–2079
86. Meng, E. C., Goddard, T. D., Pettersen, E. F., Couch, G. S., Pearson, Z. J., Morris, J. H., *et al.* (2023) UCSF ChimeraX: tools for structure building and analysis. *Protein Sci.* **32**, e4792
87. Pettersen, E. F., Goddard, T. D., Huang, C. C., Meng, E. C., Couch, G. S., Croll, T. I., *et al.* (2021) UCSF ChimeraX: structure visualization for researchers, educators, and developers. *Protein Sci.* **30**, 70–82